

Available at www.sciencedirect.com

SciVerse ScienceDirect

journal homepage: www.elsevier.com/locate/carbon

One-pot synthesis of uniform Fe_3O_4 nanocrystals encapsulated in interconnected carbon nanospheres for superior lithium storage capability

Naiqin Zhao, Shan Wu, Chunnian He ^{*}, Zhiyuan Wang, Chunsheng Shi, Enzo Liu, Jiajun Li

School of Materials Science and Engineering and Tianjin Key Laboratory of Composites and Functional Materials, Tianjin University, Tianjin 300072, China

ARTICLE INFO

Article history:

Received 9 November 2012

Accepted 19 January 2013

Available online 29 January 2013

ABSTRACT

Uniform and small Fe_3O_4 nanocrystals (~ 9 nm) encapsulated in interconnected carbon nanospheres (~ 60 nm) for a high-rate Li-ion battery anode have been fabricated by a one-step hydrothermal process followed by annealing under Ar, which can be applied for the preparation of a number of metal oxide nanocrystals encapsulated in interconnected carbon nanospheres. The as-synthesized interconnected $\text{Fe}_3\text{O}_4/\text{C}$ nanospheres displayed high performance as an anode material for Li-ion battery, such as high reversible lithium storage capacity (784 mA h/g at 1 C after 50 cycles), high Coulombic efficiency ($\sim 99\%$), excellent cycling stability, and superior rate capability (568 mA h/g at 5 C and 379 mA h/g at 10 C) by virtue of their unique structure: the nanosized Fe_3O_4 nanocrystals encapsulated in interconnected conductive carbon nanospheres not only endow large quantity of accessible active sites for lithium ion insertion as well as good conductivity and short diffusion length for lithium ion transport but also can effectively circumvent the volume expansion/contraction associated with lithium insertion/extraction.

© 2013 Elsevier Ltd. All rights reserved.

1. Introduction

Lithium ion batteries (LIBs) have been extensively used in portable electronic devices due to their high energy density and long cycle life. In recent years, the ever-increasing and urgent demand for the widespread application in hybrid electric vehicles (HEVs) and plug-in hybrid electric vehicles (PHEVs) has largely promoted the global research interests to develop LIBs with high reversible capacity, excellent rate capability and cycling stability [1–5]. However, graphite, the currently used anode material for commercial LIBs, has already approached its theoretical limit (372 mA h/g). Therefore, seeking alternative anode materials has become an urgent task now-

adays. Among the feasible anode materials, Fe_3O_4 has been proven to be a possible candidate due to its high theoretical capacity (924 mA h/g), nontoxicity, high corrosion resistance, low cost, natural abundance and environmental friendliness. The capacity of lithium storage is mainly achieved through the reversible conversion reaction between lithium ion and Fe_3O_4 , forming Fe nanocrystals dispersed in Li_2O matrix [5,6]. Despite of those intriguing features, Fe_3O_4 still suffers from rapid capacity fading and poor cyclability that is caused by the drastic volume expansion and contraction during lithium insertion/extraction. The low conductivity of Fe_3O_4 also induces additional performance degradation, especially when charging and discharging at high current densities.

^{*} Corresponding author. Fax: +86 22 27891371.

E-mail address: cnhe08@tju.edu.cn (C. He).

0008-6223/\$ - see front matter © 2013 Elsevier Ltd. All rights reserved.

<http://dx.doi.org/10.1016/j.carbon.2013.01.056>

There have been a number of recent reports describing possible approaches to circumvent the issues posed by the unsatisfactory conductivity, and severe volume change of Fe_3O_4 . One of them is to utilize nanometer-scale particles with designed morphology, such as nanospheres, nanowires, nanorods, nanotubes, and hollow nanostructures, for improving the electrochemical response of the electrodes [4–8]. It is in fact expected that the passage from bulk to nanostructures results in shorter path lengths for lithium ion transport and accommodation of the mechanical strain of lithium ion insertion/extraction. However, there has been limited success in producing Fe_3O_4 nanostructured electrodes with satisfactory high specific capacity and high rate capability. Another effective approach in tackling the above problems is the creation of carbon-based composites containing the active material of Fe_3O_4 . For instance, some groups have synthesized Fe_3O_4 nanospheres with carbon matrix support [9] and carbon-coated Fe_3O_4 nanostructures [10–14] to improve electrochemical performances. The others have employed porous carbon [15–18] or graphene or/and carbon nanotubes [19–24] as substrate materials for synthesis of captive nanoparticles confined in or bonded to the carbon. An advantage of this method is that it is applicable to a variety of metal oxides such as Fe_3O_4 , Fe_2O_3 , NiO and Co_3O_4 , etc. It is hypothesized that the introduced carbon matrices not only function as a structural buffering layer to cushion the mechanical stress caused by the large volume change of Fe_3O_4 during the charge–discharge process, but also act as a robust network to preserve good electronic conductivity of the overall electrode. Although a great success has been achieved in designing and preparing Fe_3O_4 /carbon composites with relatively high specific capacity and cyclability at lower charge/discharge rates when used as anode materials for LIBs, the preparation of Fe_3O_4 /carbon composite electrodes with high specific capacity and cyclability at higher charge/discharge rates remains a great challenge. Recently, Dillon et al. have successfully fabricated a high-rate Li-ion anode based on a nanostructured Fe_3O_4 /SWCNT composite, which was obtained by embedding Fe_3O_4 nanoparticles uniformly in an interconnected single-walled carbon nanotube (SWCNT) net [25]. However, the production of pure SWCNTs is very expensive and difficult to scale up, which is very unfavorable for their wide application in LIBs.

Herein, we report an easy and scalable one-pot hydrothermal process followed by annealing in argon atmosphere using glucose and iron nitrate as source materials to prepare uniform and small Fe_3O_4 nanocrystals encapsulated in interconnected carbon nanospheres (designated as Fe_3O_4 @C nanospheres) for a high-rate LIB anode. This one-pot synthesis approach in situ generates uniform Fe_3O_4 nanocrystals in a confined nanospace of carbonaceous matter, which can obviate the requirement of an additional step to introduce a layer of carbon coating on the surface of the pre-synthesized iron oxide. During the electrochemical measurement, these interconnected Fe_3O_4 @C nanospheres demonstrate excellent cycling performance at 1 C (1 C = 924 mA/g) with a reversible capacity of 784 mA h/g after 50 cycles and superior rate capability, exhibiting 568 and 379 mA h/g at 5 and 10 C, respectively.

2. Experimental

2.1. Synthesis of interconnected Fe_3O_4 @C nanospheres

The reagents were purchased from Tianjin Chemical Reagent Company and used without further purification. In a typical synthesis, 0.9 g glucose ($\text{C}_6\text{H}_{12}\text{O}_6$) was dissolved in 40 mL deionized water and 1.212 g iron (III) nitrate enneahydrate ($\text{Fe}(\text{NO}_3)_3 \cdot 9\text{H}_2\text{O}$) was dissolved in 2 mL deionized water. The above two aqueous solutions were then mixed together and ultrasonicated for 15 min. The resulting mixed solution (37.5 mL) was transferred into a 40 mL Teflon-lined stainless steel autoclave, and then heated at 190 °C for 9 h. Once cooled to room temperature naturally, the resulted solid was collected through centrifugation and washed thoroughly with deionized water for several times. Subsequently, the obtained product was redispersed into a certain amount of deionized water, and freeze dried to obtain Fe_2O_3 nanocrystals encapsulated in interconnected carbon nanospheres (designated as Fe_2O_3 @C nanospheres). Finally, the interconnected Fe_2O_3 @C nanospheres were annealed at 500 °C for 2 h in a tube furnace under a flowing Ar atmosphere to obtain Fe_3O_4 nanocrystals encapsulated in interconnected carbon nanospheres (Fe_3O_4 @C nanospheres).

2.2. Characterization of the Fe_2O_3 @C and Fe_3O_4 @C nanospheres

The morphology, dimension, lattice distances, and crystallographic structures of the Fe_2O_3 @C and Fe_3O_4 @C nanospheres were studied by transmission electron microscope (TEM) and high-resolution TEM (HRTEM) performed on a FEI Tecnai G² F20 TEM. Energy-dispersive X-ray spectroscopy (EDX) analyses of a group of Fe_3O_4 @C nanospheres were carried out with spatially resolved EDX spectrum attached to the TEM. Scanning electron microscope (SEM) investigations were performed using a TDCLS-4800 SEM (Hitachi). Raman spectrum of the Fe_3O_4 @C nanospheres was recorded on the LabRAM HR Raman spectrometer using laser excitation at 514.5 nm from an argon ion laser source to validate the presence of carbon in the nanospheres. X-ray diffraction (XRD) measurements were taken on a Rigaku D/max diffractometer with Cu K α radiation at a wavelength of 1.5406 Å, and a step size of 0.02° to characterize the structure of the Fe_2O_3 @C and Fe_3O_4 @C nanospheres. JADE5 software was utilized for data analysis. The crystallite size of nanoparticles is calculated by the Scherrer equation.

$$L = 0.89\lambda / \beta(\theta) \cos \theta$$

where λ is the X-ray wavelength in nm, β is the intrinsic peak width in radians on a 2θ scale, θ is the Bragg diffraction angle, and 0.89 is the Scherrer constant. Thermogravimetric analysis (TGA) was performed with a Perkin Elmer (TA instruments) up to 1000 °C at a heating rate of 10 °C/min in air. N_2 adsorption–desorption isotherms were measured with an autosorb iQ instrument (Quantachrome U.S.) at 77 K. The Brunauer–Emmett–Teller (BET) method was utilized to calculate the specific surface areas. The pore size distributions were derived from the desorption branches of the isotherms based on the Barrett–Joyner–Halanda (BJH) model.

2.3. Electrochemical measurements

The electrochemical measurements were conducted using coin-type test cell (CR2032) with lithium metal working as both counter and reference electrode. The working electrodes were prepared by the following steps: 80 wt.% active materials ($\text{Fe}_3\text{O}_4\text{@C}$ nanospheres, bare carbon without Fe_3O_4 or commercial Fe_3O_4 nanoparticles with an average diameter of 20 nm purchased from DK nanotechnology Co. LTD, Beijing), 10 wt.% conductivity agent (carbon black) and 10 wt.% binder (polyvinylidene fluoride, PVDF) were blended with N-methylpyrrolidone as a solvent. Electrode film was prepared by coating the mixture on a copper foil and dried successively in a vacuum oven at 80 °C for 4 h first and then 120 °C for 12 h. A Celgard 2400 polypropylene membrane was used as the separator. 1.0 M LiPF_6 in an ethylene carbonate/dimethyl carbonate (EC/DMC/DEC) mixture (1:1:1 v/v/v) was used as the electrolyte. The assembly of the cell was conducted in an argon-filled glove box. Cyclic voltammetry (CV) measurement was conducted at 0.1 mV/s within the range of 0.01–3.0 V on CHI660D electrochemical workstation. Galvanostatic charge/discharge tests were performed on Land CT2001A (China) at different current densities with the potential between 0.005 and 3.00 V (vs. Li/Li^+). All the specific capacities here were calculated on the basis of the total weight of the $\text{Fe}_3\text{O}_4\text{@C}$ nanospheres, the bare carbon or the commercial Fe_3O_4 nanoparticles.

3. Results and discussion

Our novel fabrication process for interconnected $\text{Fe}_3\text{O}_4\text{@C}$ nanospheres principally consists of two steps, as shown in Fig. 1A. The first step involves producing uniform and ultrasmall Fe_2O_3 nanocrystals encapsulated in interconnected carbon nanospheres through hydrothermal treatment on aqueous solution containing iron nitrate (0.075 mol/L) and glucose (0.125 mol/L) at 190 °C for 9 h. It has been reported that when glucose was hydrothermally carbonized at 160–200 °C, carbonaceous spheres of tunable sizes in the nano- to micrometer range were

synthesized. During the hydrothermal process, the glucose molecules underwent dehydration, condensation, or polymerization and aromatization reactions, leading to carbonaceous spheres, which consist of a highly aromatic nucleus (hydrophobic) and a hydrophilic shell containing a high concentration of reactive oxygen functional groups (i.e., hydroxyl/phenolic, carbonyl, or carboxylic) [26,27]. Furthermore, hydrothermal carbonization of glucose in the presence of inorganic salts can give rise to the formation of core/shell metal/carbon hybrid materials (such as Ag@C , Cu@C , Au@C , etc.) [26,28–30]. As for the inorganic salt of iron nitrate, it can be transformed to $\alpha\text{-Fe}_2\text{O}_3$ nanocrystals during the hydrothermal treatment, which are tend to bind with the surface functional groups of the carbon colloids derived from glucose through the Coulombic interaction [31,32]. Inspired by these previous works, we designed a one-pot hydrothermal reaction using glucose and iron nitrate as source materials and successfully produced interconnected carbon nanospheres with uniform and ultrasmall $\alpha\text{-Fe}_2\text{O}_3$ nanocrystals encapsulated (designated as $\text{Fe}_2\text{O}_3\text{@C}$). The speculated formation process of the $\text{Fe}_2\text{O}_3\text{@C}$ nanospheres is shown in Fig. 1B. During the initial stage of the hydrothermal carbonization, dehydration of glucose results in very small carbonaceous colloids with a low degree of polymerization and hydrolysis of iron nitrate leads to FeOOH [31], which further is reduced to uniform $\alpha\text{-Fe}_2\text{O}_3$ nanocrystals by hydrogen released from the carbonization process [33]. The $\alpha\text{-Fe}_2\text{O}_3$ nanocrystals then combine with very small carbonaceous colloids through Coulombic interactions and condense to generate carbon nanospheres with Fe_2O_3 nanocrystals encapsulated. Moreover, it is also found that the size of the carbon nanospheres and the content of the Fe_2O_3 nanocrystals can be tuned by adjusting the experimental parameters, such as the reaction temperature, reaction time and the initial ratio between iron nitrate and glucose. With a lower temperature, shorter time and lower initial ratio of iron nitrate to glucose, smaller carbon nanospheres with less Fe_2O_3 nanocrystals encapsulated can be obtained, as shown in Fig. S1. In the second step, the interconnected $\text{Fe}_2\text{O}_3\text{@C}$ nanospheres are annealed at 500 °C for 2 h in Ar to in situ yield uniform and small Fe_3O_4 nanocrystals

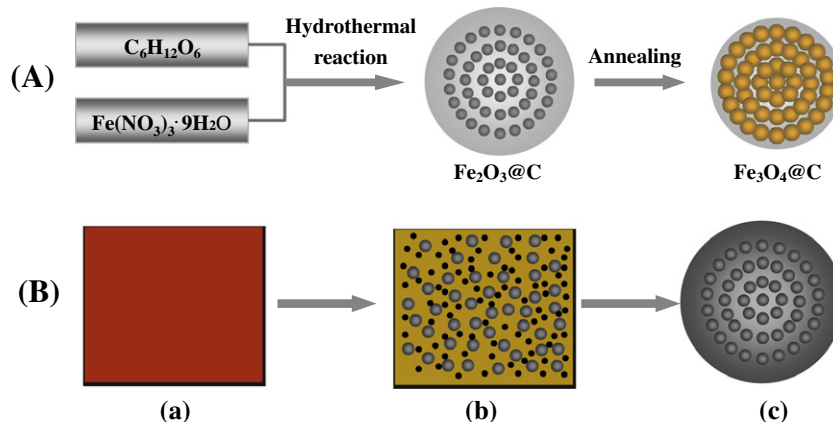


Fig. 1 – Scheme of the formation process of (A) uniform and small Fe_3O_4 nanocrystals encapsulated in the carbon nanosphere and (B) uniform and ultrasmall Fe_2O_3 nanocrystals encapsulated in the carbon nanosphere: (a) aqueous solution of iron nitrate and glucose, (b) iron oxide nanocrystals (gray dots) and small carbonaceous colloids (black dots) formed during the initial stage of the hydrothermal carbonization, (c) carbon nanosphere with uniform and ultrasmall Fe_2O_3 nanocrystals encapsulated.

encapsulated in interconnected carbon nanospheres due to that the inner hematite cores can be reduced to magnetite by the outer carbon layers (Fig. 1A). The source materials and the synthetic processes are both viable for large-scale production, making this approach particularly attractive for practical applications.

The crystallographic structure, morphology and microstructure of the hydrothermal product ($\text{Fe}_2\text{O}_3/\text{C}$ nanospheres) are determined by XRD, SEM and TEM, as shown in Fig. 2. From XRD pattern of Fig. 2(a), we can see that all of the diffraction peaks could be indexed to the rhombohedral phase of hematite ($\alpha\text{-Fe}_2\text{O}_3$) (JCPDS No. 33-0664) and the broadness of the diffraction peaks indicates the small size and not well crystallized feature of the Fe_2O_3 nanocrystals. According to the Scherrer's formula, the average crystallite size of the Fe_2O_3 phase is found to be ~ 3.8 nm. The broad signal in the range of $20\text{--}30^\circ$ may be due to the presence of non-crystalline carbon in the hydrothermal product, because the most intense reflection for graphitic carbon (002 layer) should appear at about 26.8° .

Fig. 2(b) shows a typical SEM image of the hydrothermal product. It can be observed that this sample exhibits spherical nanoparticles with an average diameter of ~ 65 nm and a narrow size distribution. A closer examination revealed that a majority of these nanospheres is interconnected, resulting in porous self-assembled structure with rough surface. In order to unveil the microstructure of these nanospheres, the sample was characterized by TEM, as shown in Fig. 2(c–d). A low-magnification TEM image in Fig. 2(c) presents that the nanospheres, which exhibit an apparent core-shell nanostructure, are indeed interconnected. A high-magnification TEM image of Fig. 2(d) reveals that the outer carbon layer with a thickness of 5–15 nm is amorphous, and the inner hematite

core is actually composed of dozens of tiny Fe_2O_3 nanocrystals with a size of ~ 4 nm, in agreement with above XRD result.

The interconnected characteristic of $\text{Fe}_2\text{O}_3/\text{C}$ nanospheres enable their composition of individual components to be varied without damaging the overall structure. By careful annealing at 500°C for 2 h in Ar, $\text{Fe}_3\text{O}_4/\text{C}$ nanospheres can be derived through phase transformation of Fe_2O_3 to Fe_3O_4 , which was confirmed by the color variation from brown to totally black and the strong ferromagnetism of the final black products after annealing, and the following XRD analysis and TEM observations. The XRD pattern (Fig. 2(a)) of the $\text{Fe}_3\text{O}_4/\text{C}$ nanospheres exhibits diffraction peaks of Fe_3O_4 nanocrystals which matched very well with those of magnetite (JCPDS No. 19-0629). The strong diffraction peaks indicate good crystallinity of the Fe_3O_4 phase. The average particle size of Fe_3O_4 nanocrystals calculated from the largest diffraction peak (311) by using the Scherrer's formula is estimated to ~ 9.14 nm. However, no diffraction peak of graphite was detected in the XRD pattern, indicating the not well crystallized nature of the carbon layer.

Typical SEM and TEM images provide insight into the morphology and microstructure of the final product ($\text{Fe}_3\text{O}_4/\text{C}$ nanospheres). Fig. 3(a) displays a typical SEM image of nanospheres prepared by calcinating $\text{Fe}_2\text{O}_3/\text{C}$ nanospheres at 500°C for 2 h under Ar. The spheres are uniform and interconnected, virtually indistinguishable from $\text{Fe}_2\text{O}_3/\text{C}$ nanospheres prepared by hydrothermal reaction, except for the slight decrease of roughness and diameter because of the reduction of Fe_2O_3 to Fe_3O_4 by the outer carbon layer during the thermal treatment process. Importantly, it should be noted that the interconnected structure of the $\text{Fe}_3\text{O}_4/\text{C}$ nanospheres is favorable for achieving high durability and high rate capability when used as a LIB anode [25]. Fig. 3(b–d) show TEM images of the $\text{Fe}_3\text{O}_4/\text{C}$ nanospheres, which further verify the

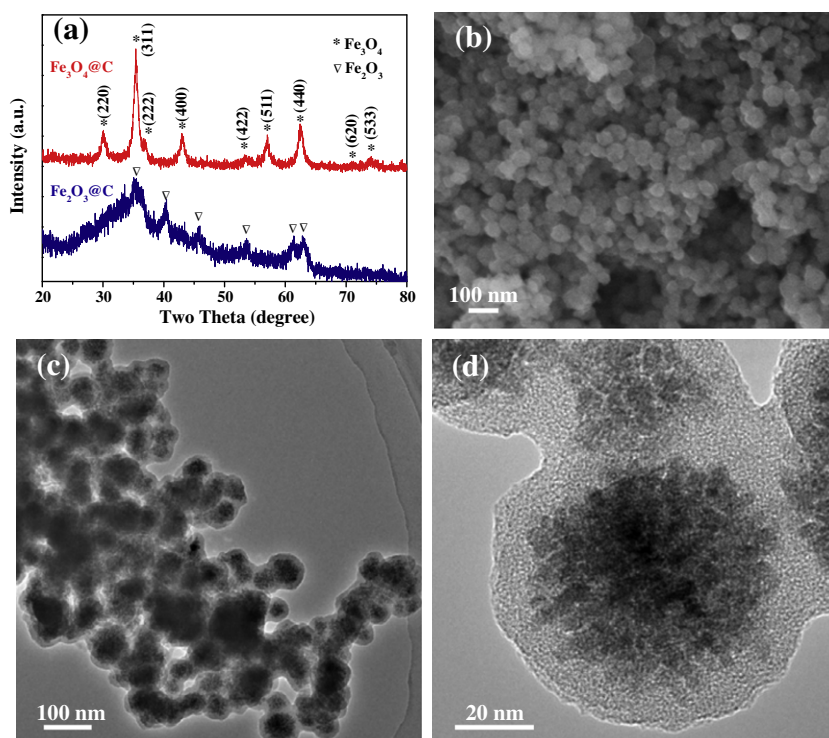


Fig. 2 – (a) XRD patterns of the $\text{Fe}_2\text{O}_3/\text{C}$ and $\text{Fe}_3\text{O}_4/\text{C}$ nanospheres. (b–d) SEM and TEM images of the $\text{Fe}_2\text{O}_3/\text{C}$ nanospheres.

interconnected structure of these nanospheres. As can be seen, the outer partially graphitic carbon layer with a thickness of 3–8 nm is uniform and continuous, and the inner magnetite cores with average diameter of ~50 nm consist of several Fe_3O_4 nanocrystals with an average size of ~9 nm. The lattice d -spacings of 0.483 and 0.252 nm corresponding to (111) and (311) planes of Fe_3O_4 , respectively, are identified in Fig. 3(c and d). In order to quantify the weight percentage of Fe_3O_4 in these nanospheres, TGA was carried out and the data are shown in Fig. 4(a). The material is heated to 1000 °C under air so that Fe_3O_4 is oxidized to Fe_2O_3 and carbon is oxidized to CO_2 . From the remaining weight of Fe_2O_3 , the original weight fraction of Fe_3O_4 is calculated to be 62.64%.

The as-obtained $\text{Fe}_3\text{O}_4@\text{C}$ nanospheres were also characterized by Raman spectroscopy in detail to further validate the presence of partially graphitic carbon on the Fe_3O_4 nanocrystals. Representative Raman spectrum is shown in Fig. 4(b). The spectrum was collected within the 800–2000 cm^{-1} range, corresponding to the spectral region that provides the most valuable data on the structure of carbon materials. The recorded spectrum shows two broad Raman bands at about 1365 and 1589 cm^{-1} . The latter band corresponds to the E_{2g} mode (stretching vibrations) in the basal plane of the crystalline graphite (G graphitic peak). The width of the G-band is related to the extent of disorder within the carbon sp^2 plane graphene layer. The band located at 1365 cm^{-1} (D-band) is associated with disorder, it being allowed by zone edge modes of the graphite structure that becomes active due to the lack of long range order in amorphous and quasi-crystalline forms of carbon materials. The peak intensity ratio between D and G

bands (I_D/I_G) generally provides a useful index for comparing the degree of crystallinity of various carbon materials, i.e., smaller the ratio of I_D/I_G , higher the degree of ordering in the carbon material. The I_D/I_G ratio for our $\text{Fe}_3\text{O}_4@\text{C}$ nanospheres was calculated to be ~0.86, demonstrating that the carbon in the nanospheres we obtained is partially graphitic, which will be beneficial for achieving better electronic conduction between adjacent Fe_3O_4 nanocrystals. Nitrogen adsorption-desorption measurements are carried out at 77 K to study the textural characteristics of the $\text{Fe}_3\text{O}_4@\text{C}$ nanospheres. As shown in Fig. 4(c), the isotherm profile of the sample can be categorized as type I with small a hysteresis loop observed at a relative pressure of 0.9–1.0, indicating that the pores inside the sample consist of micropores and mesopores, as further verified by the pore size distribution in Fig. 4(d). The BET specific surface area is measured to be 191.16 m^2/g , which is much higher than that of commercial Fe_3O_4 nanoparticles (about 2 m^2/g). It is believed that the relatively large specific surface area is beneficial for electrolyte access [20]. The nitrogen adsorption/desorption isotherm study (Fig. 4(d)) shows that the pores inside the sample consist of mesopores and micropores and the pore size distribution lies in 0.6–34.5 nm range. The pore volume of the product determined by the Barrett-Joyner-Halenda method is 0.63 cm^3/g . Combining the result with SEM measurements, the porous structure containing mesopores may benefit to the electrolyte ion diffusion to active sites with less resistance and tolerate the volume change of the Fe_3O_4 nanocrystals during charge/discharge cycles [20,34].

Fig 5 shows the electrochemical performance of the $\text{Fe}_3\text{O}_4@\text{C}$ nanospheres. As shown in Fig. 5(a), CV was applied

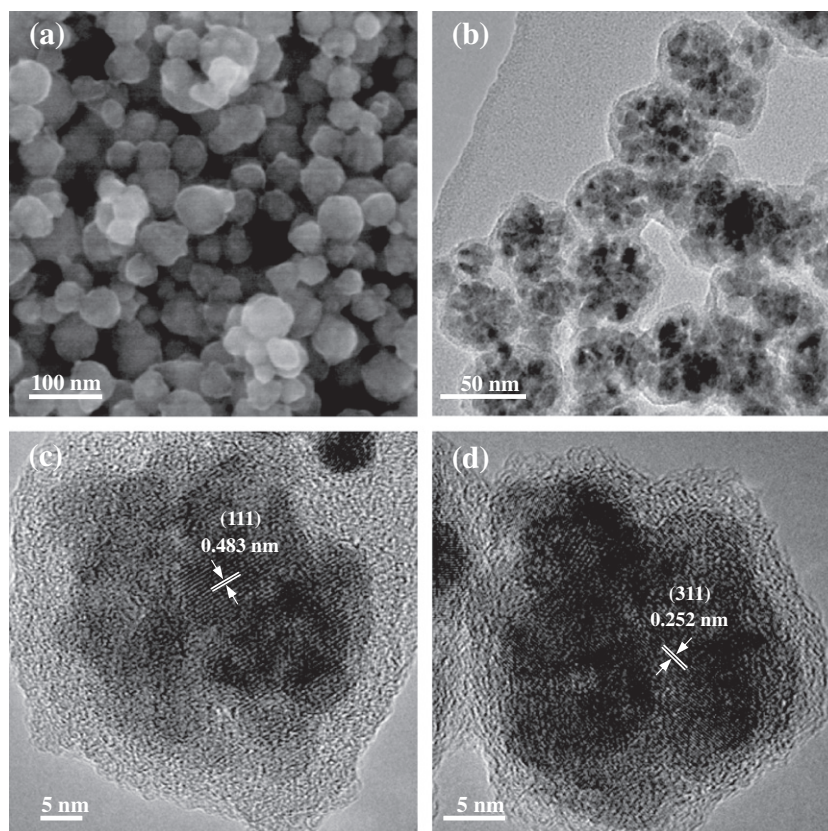


Fig. 3 – (a) SEM image of the $\text{Fe}_3\text{O}_4@\text{C}$ nanospheres. (b–d) TEM images of the $\text{Fe}_3\text{O}_4@\text{C}$ nanospheres.

to investigate the electrochemical details when the cell was set to be scanned at 0.1 mV/s within the voltage window of 0.01–3.00 V (vs. Li/Li⁺). The patterns are consistent with the CV results from other reports on Fe₃O₄-C composites [13,15–19]. Two cathodic peaks at voltage potentials of 0.97 and 0.68 V are observed in the first cathodic scan, while they disappeared in the following scans, which is due to the irreversible formation of a solid electrolyte interface (SEI) and the decomposition of electrolyte [13,15–19]. In subsequent cycles, the cathodic peak shifts to 0.83 V and tends to be stable, indicating the high Coulombic efficiency and the stable and good reversibility of the sample. In the anodic scans, two small peaks at 1.62 and 1.88 V are recorded. These cathodic and anodic peaks correspond to the electrochemical reduction/oxidation (Fe₃O₄ ↔ Fe) reactions accompanying Lithium ion insertion (lithiation) and extraction (delithiation) [13,15–19].

Fig. 5(b) presents the charge/discharge profiles of the Fe₃O₄@C nanospheres in the 1st, 2nd, 10th, 20th, 30th, 40th, and 50th cycles at a current density of 924 mA/g. The first discharge capacity is 1528 mA h/g, but the first charge capacity is 1096 mA h/g, leading to a relatively low Coulombic efficiency of 71.7%. The relatively low initial Coulombic efficiency may be caused by the irreversible capacity loss, including inevitable formation of SEI and decomposition of electrolyte, which are common to most anode materials [9–24]. This characteristic also agrees well with the CV result that the cathodic peaks are present in the first scan while absent afterward. The discharge voltage plateau at ~0.84 V in the first cycle is different

from those of other cycles at ~1.0 V, further indicating that irreversible reactions occurred in the first cycle. In the second cycle, the Coulombic efficiency increases to 94.2% and a discharge capacity of 1087 mA h/g is achieved (as shown in Fig. 5(c)), which is higher than the theoretical value for Fe₃O₄ (924 mA h/g). Similar results have been reported for many other transition metal oxides [35,36]. It is reported that the reaction of oxygen-containing functional groups on carbon with lithium ions can also contribute to the lithium storage capacity [20,11]. Besides, the reversible decomposition of the electrolyte with the formation of SEI and extra lithium ion adsorption/desorption on the SEI while cycling may lead to the high experimental lithium storage capacity, as well [4]. Note that the charge curve is a sloping curve with no obvious voltage platform, owing to the large surface area induced during the former discharge process which could widen the reaction site energy range for intercalation compounds, [37,38] or the amorphous character of the active materials itself [39].

The comparative cycling performance between the Fe₃O₄@C nanospheres and commercial Fe₃O₄ nanoparticles at a current density of 924 mA/g is illustrated in Fig. 5(c). Apparently, the Fe₃O₄@C sample demonstrates a much better cyclic retention than the commercial Fe₃O₄ nanoparticles, with a high reversible capacity of 811 mA h/g after 20 cycles and 784 mA h/g even after 50 cycles. Furthermore, their Coulombic efficiency is maintained at ~99% after the 12th cycle. For the commercial Fe₃O₄ nanoparticles with average diameter of about 20 nm, their capacity fades very rapidly during the

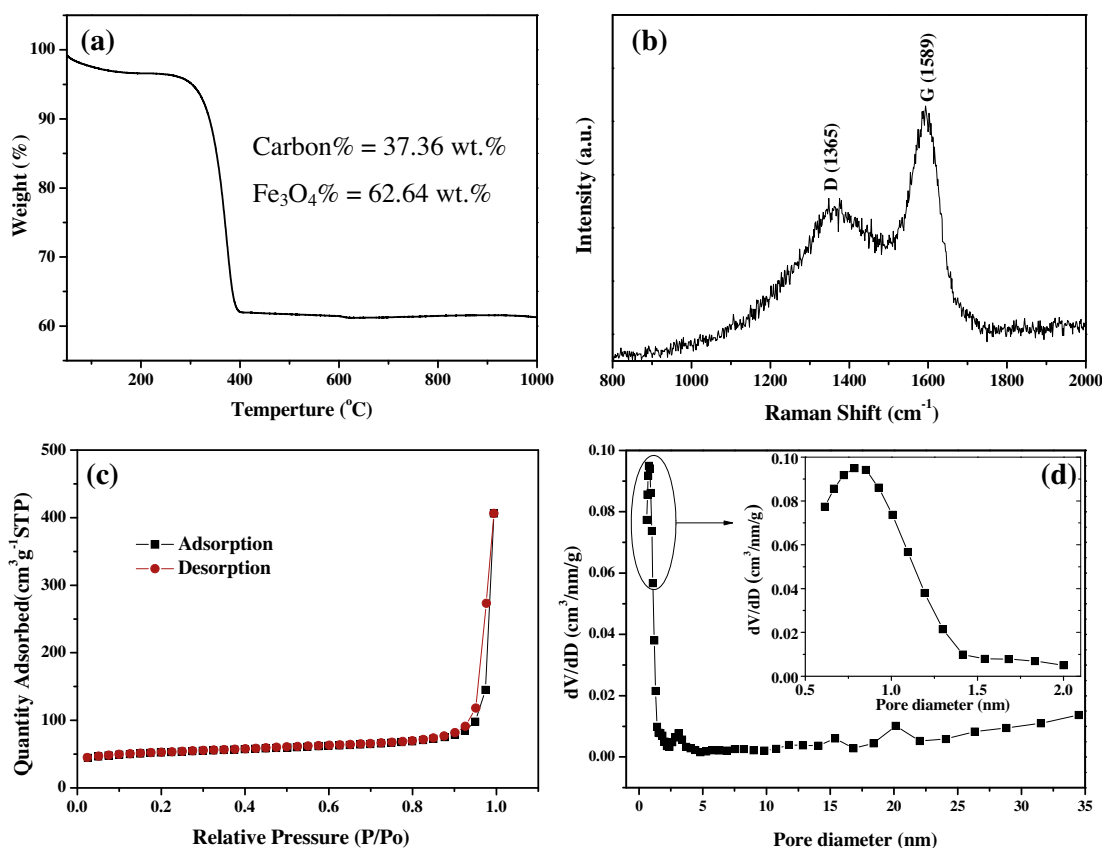


Fig. 4 – (a) TGA curve, (b) Raman spectrum, (c) nitrogen adsorption-desorption isotherms and (d) pore size distribution curve of the Fe₃O₄@C nanospheres, inset of (d) magnification of pore size distribution between 0.5 and 2.0 nm.

course of the first few cycles. Compared to the $\text{Fe}_3\text{O}_4/\text{C}$ nanospheres, a much lower capacity of only 260 mA h/g is delivered at the end of the 38 cycles. This evidently proves that the remarkably positive effect of the interconnected carbon layer in the nanospheres. It is well-known that during the charge–discharge process, the Fe_3O_4 -based anode surface would be covered by a solid-electrolyte interphase (SEI) film, which forms due to the reductive decomposition of the organic electrolyte [9–24]. For the $\text{Fe}_3\text{O}_4/\text{C}$ nanospheres, a thin passivating SEI can form around the outer carbon layer during the first few cycles, and its further formation is terminated due to the electronically insulating nature of the SEI. Meanwhile, during the formation of a stable thin SEI around the outer carbon layer in the first few cycles, the capacity of the anode of $\text{Fe}_3\text{O}_4/\text{C}$ nanospheres degrades rapidly [10,13,15,16]. After the formation of a stable SEI, their capacity maintains well and thus the anode of $\text{Fe}_3\text{O}_4/\text{C}$ nanospheres presents excellent cycling performance. However, in the case of bare Fe_3O_4 nanoparticles, the SEI will rupture due to the mechanical strain generated by the volume expansion/contraction during cycling and thus the electrode surface would be cyclically exposed to the electrolyte, which results in continual formation of very thick SEI films and accordingly continual consuming of electrolyte. The cyclically rupture and growth of SEI can cause low Coulombic efficiency, higher resistance to ionic transport, and low electronic conductivity of the whole electrode. Therefore, the capacity of the anode of bare Fe_3O_4 nanoparticles de-

creases rapidly and their cycling performance is much worse than that of the $\text{Fe}_3\text{O}_4/\text{C}$ nanospheres. In order to further investigate the effect of the outer carbon layer on the electrochemical performance of the $\text{Fe}_3\text{O}_4/\text{C}$ nanospheres, we also tested the cycling performance of the bare carbon obtained by removing the Fe_3O_4 from the $\text{Fe}_3\text{O}_4/\text{C}$ nanospheres, the result is shown in Fig. 5c. As can be seen, the bare carbon shows a very low capacity of about 210 mA h/g, but its cycling performance is very excellent. This indicates that the outer carbon layer might contribute little to the Li-storage capacity of the $\text{Fe}_3\text{O}_4/\text{C}$ nanospheres, but be very beneficial for improving the structural stability of the $\text{Fe}_3\text{O}_4/\text{C}$ nanospheres.

Besides their outstanding reversible capacity and cycling stability, these $\text{Fe}_3\text{O}_4/\text{C}$ electrodes also exhibit impressive rate performance. Fig. 5(d) shows the rate capability of $\text{Fe}_3\text{O}_4/\text{C}$ electrode: after the rate was increased to 10 C (9240 mA/g) and capacities were recorded, the charge–discharge rates were reduced from 9240 (10 C) to 92.4 mA/g (0.1 C) again. It can be seen that the charge and discharge capacities decrease as the charge–discharge rates increase, which is caused by the low diffusion rate of the lithium ion into anodes at high rates [3–5]. However, the $\text{Fe}_3\text{O}_4/\text{C}$ anode maintains much more stable charge and discharge capacities at higher rates (1, 2, 5 and 10 C) than that at lower rates (0.1 and 0.2 C). This phenomenon is also shown in other works [22–24]. According to the kinetics equation of electrode material, i.e. $\tau = L^2/2D$, where τ is the diffusion time, L is the diffusion distance, and D is the Li^+ chemical diffusion coefficient,

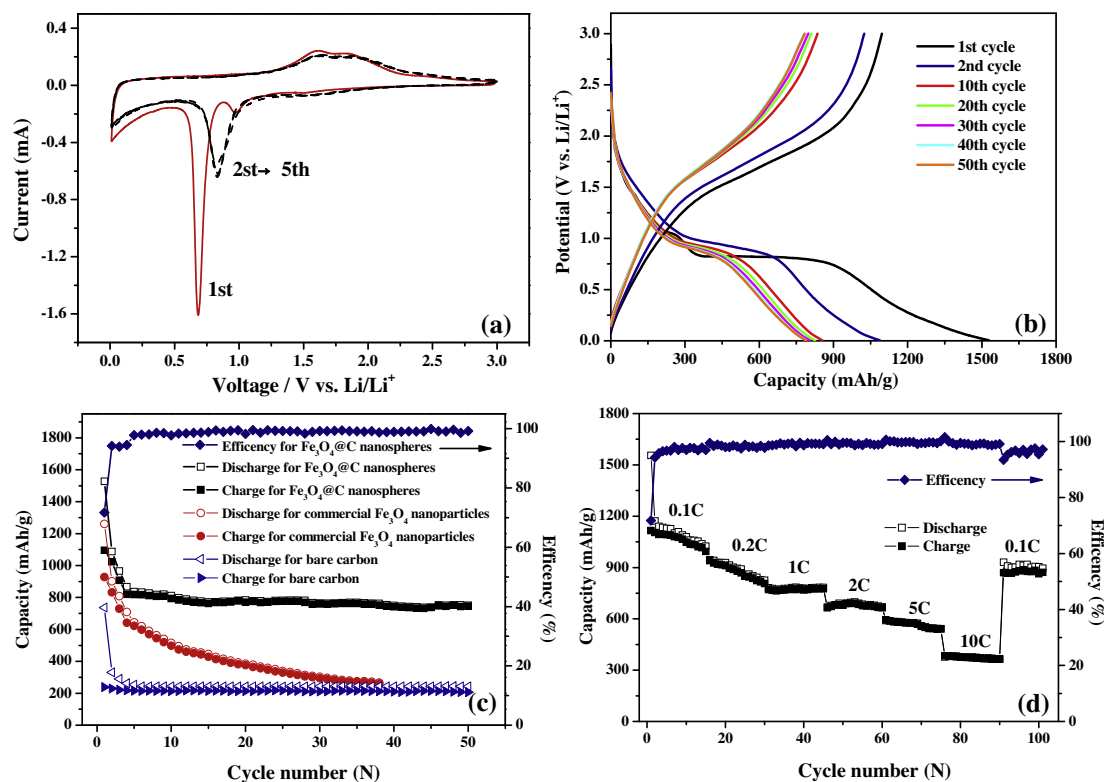


Fig. 5 – (a) CV of the interconnected $\text{Fe}_3\text{O}_4/\text{C}$ nanospheres in a voltage range of 0.01–3.0 V at a scanning rate of 0.1 mV/s. (b) Discharge/charge voltage profiles cycled at the 1st, 2nd, 10th, 20th, 30th, 40th, and 50th cycle of the $\text{Fe}_3\text{O}_4/\text{C}$ nanospheres between 0.005 and 3.00 V at a current density of 924 mA/g. (c) Comparative cycling performance of interconnected $\text{Fe}_3\text{O}_4/\text{C}$ nanospheres, commercial Fe_3O_4 nanoparticles and bare carbon without Fe_3O_4 at a current density of 924 mA/g. (d) The rate capability of interconnected $\text{Fe}_3\text{O}_4/\text{C}$ nanospheres at the rates between 0.1 and 10 C (1 C = 924 mA/g).

cient [40], when the electrode material is charged and discharged at lower rates, the diffusion time (τ) is longer than that at higher rates, which leads to the higher specific capacity. Meanwhile, the longer diffusion time (τ) can also inevitably cause the volume change of the electrode materials and the structure degradation. Therefore, the discharge capacity is fading fast with the increase of the cycle numbers. However, in the case of charging and discharging at higher rates, the Li^+ insertion/extraction just occurs near the surface of the electrode material and thus the Li^+ diffusion distance is much shorter, this induces the increase of kinetics performance and maintains the structure stable. Although the capacity is lower, the cycling stability of the electrode material is much better than that at lower rates. The rates and average reversible capacities at different rates are presented in Table S1. It can be seen that the average reversible capacities are 1064, 875, 771, 678, 568, and 379 mA h/g at the rates of 0.1 (step 1), 0.2 (step 2), 1 (step 3), 2 (step 4), 5 (step 5), and 10 C (step 6), respectively, which evidently demonstrates that the $\text{Fe}_3\text{O}_4/\text{C}$ nanospheres display superior capacity retention at higher rates. Even at a high rate of 10 C (9240 mA/g at step 6), charging/discharging finished within 6 min still gave a average reversible capacity to be 379 mA h/g, equivalent to about 35.6% of capacity using 0.1 C (step 1). Upon returning to 0.1 C (step 7), stable capacity of 870 mA h/g was resumed and negligible capacity loss was observed after another 10 cycles. Overall, this electrode retained about 82.1% of the capacity over 100 cycles. Such remarkable high-rate performance, high specific capacity and cycling stability at high charge/discharge rates are higher than in previously reported work on $\text{Fe}_3\text{O}_4/\text{carbon}$ composites [9–24].

TEM techniques were employed to examine the morphology evolution of the $\text{Fe}_3\text{O}_4/\text{C}$ anode under the severe volume expansion and contraction during lithium insertion/extraction. Fig. S2 shows the TEM images of the $\text{Fe}_3\text{O}_4/\text{C}$ anode after 100 charge/discharge cycles for rate performance test in Fig. 5(d). Compared with Fig. 3, the morphology of the $\text{Fe}_3\text{O}_4/\text{C}$ after 100 charge/discharge cycles was similar to that of the pristine one. Moreover, TEM images in Fig. S2(c) and (d) show that the carbon layer and the core-shell structure still maintained after charge/discharge cycling, and the thickness of the carbon layer was similar to that of before cycling. The similar morphology indicates that the $\text{Fe}_3\text{O}_4/\text{C}$ anodes can effectively decrease substantial aggregation and cracking upon cycling. In particular, thin carbon layer has good elasticity to effectively accommodate the mechanical stress caused by the large volume change of Fe_3O_4 during the charge–discharge process [10–14].

As shown in the results presented above, our $\text{Fe}_3\text{O}_4/\text{C}$ electrode displays superior electrochemical performance and structural stability. These outstanding properties arise from the structure advantages of the nanospheres: the nanosized Fe_3O_4 nanocrystals (~ 9 nm) encapsulated in interconnected conductive carbon nanospheres (~ 60 nm) not only endow large quantity of accessible active sites for lithium ion insertion but also good conductivity and short diffusion length for lithium ion transport, which are beneficial for high capacity and rate capability. Meanwhile, the interconnected carbon layer is a self-supporting framework, which can not only effectively inhibit the aggregation of Fe_3O_4 nanoparticles as well as simultaneously circumvent the severe volume expansion/contraction associated with lithium insertion/extraction, but also maintain structural integrity of the electrode during charge-dis-

charge process, which are favorable to high capacity as well as cycling stability. As a consequence, their original morphology in terms of shape, size, and structural integrity can be well preserved after being charged/discharged over 100 cycles (Fig. S2). Benefit from the enhanced structural stability and integrity and excellent kinetics for lithium ion and charge transport, the lithium storage properties of our $\text{Fe}_3\text{O}_4/\text{C}$ nanospheres are thus remarkably improved.

4. Conclusions

We have successfully synthesized homogeneous and small Fe_3O_4 nanocrystals (~ 9 nm) encapsulated in interconnected carbon nanospheres (~ 60 nm) for a high-rate LIB anode by an easy one-step hydrothermal process followed by annealing in argon atmosphere. The small size of the Fe_3O_4 nanocrystals in the nanospheres allows for fast lithium ion diffusion and the interconnected structure of the carbon nanospheres can effectively circumvent the severe volume expansion/contraction associated with lithium insertion/extraction and maintain structural integrity of the electrode during charge–discharge process. Therefore, this unique structure demonstrates high reversible capacity (784 mA h/g at 1 C, 1 C = 924 mA/g), high Coulombic efficiency ($\sim 99\%$), excellent cycling stability and superior rate capacities of 568 mA h/g at 5 C and 379 mA h/g at 10 C. Both the source materials (glucose and iron nitrate) and the preparation processes used in this work are cost-effective and easy to scale up. Therefore, it has a good potential to be used for large scale applications. Furthermore, the approach reported in this work is also applicable to other metal oxide nanocrystals encapsulated in interconnected carbon nanospheres, which may find important applications as electrodes, catalysts, adsorbents, and sensors in many scientific disciplines.

Acknowledgements

The authors acknowledge the financial support by the National Natural Science Foundation of China (No. 51071107, No. 51002188 and No. 51272173) and Foundation for the Author of National Excellent Doctoral Dissertation of China (No. 201145), Natural Science Foundation of Tianjin City (No. 12JCYBJC11700), Program for New Century Excellent Talents in University, Elite Scholar Program of Tianjin University and National Basic Research Program of China (2010CB934700).

Appendix A. Supplementary data

Supplementary data associated with this article can be found, in the online version, at <http://dx.doi.org/10.1016/j.carbon.2013.01.056>.

REFERENCES

- [1] Dunn B, Kamath H, Tarascon JM. Electrical energy storage for the grid: a battery of choices. *Science* 2011;334:928–35.
- [2] Gohier A, Laïk B, Kim KH, Maurice JL, Pereira-Ramos JP, Cojocaru CS, et al. High-rate capability silicon decorated

- vertically aligned carbon nanotubes for Li-ion batteries. *Adv Mater* 2012;24:2592–7.
- [3] Tarascon JM, Armand M. Issues and challenges facing rechargeable lithium batteries. *Nature* 2001;414:359–67.
 - [4] Poizot P, Laruelle S, Grugeon S, Dupont L, Tarascon JM. Nano-sized transition-metal oxides as negative-electrode materials for lithium-ion batteries. *Nature* 2000;407:496–9.
 - [5] Taberna PL, Mitra S, Poizot P, Simon P, Tarascon JM. High rate capabilities Fe_3O_4 -based Cu nano-architected electrodes for lithium-ion battery applications. *Nat Mater* 2006;5:567–73.
 - [6] Cui ZM, Jiang LY, Song WG, Guo YG. High-yield gas-liquid interfacial synthesis of highly dispersed Fe_3O_4 nanocrystals and their application in lithium-ion batteries. *Chem Mater* 2009;21:1162–6.
 - [7] Maier J. Nanoionics: ion transport and electrochemical storage in confined systems. *Nat Mater* 2005;4:805–15.
 - [8] Chen Y, Xia H, Lu L, Xue JM. Synthesis of porous hollow Fe_3O_4 beads and their applications in lithium ion batteries. *J Mater Chem* 2012;22:5006–12.
 - [9] Chen JS, Zhang YM, (David) Lou XW. One-pot synthesis of uniform Fe_3O_4 nanospheres with carbon matrix support for improved lithium storage capabilities. *ACS Appl Mater Interfaces* 2011;3:3276–9.
 - [10] Zhang WM, Wu XL, Hu JS, Guo YG, Wan LJ. Carbon coated Fe_3O_4 nanospindles as a superior anode material for lithium-ion batteries. *Adv Funct Mater* 2008;18:3941–6.
 - [11] Muraliganth T, Murugan AV, Manthiram A. Facile synthesis of carbon-decorated single-crystalline Fe_3O_4 nanowires and their application as high performance anode in lithium ion batteries. *Chem Commun* 2009;7360–2.
 - [12] Yuan SM, Li JX, Yang LT, Su LW, Liu L, Zhou Z. Preparation and lithium storage performances of mesoporous Fe_3O_4 @C microcapsules. *ACS Appl Mater Interfaces* 2011;3:705–9.
 - [13] Zhu T, Chen JS, (David) Lou XW. Glucose-assisted one-pot synthesis of FeOOH nanorods and their transformation to Fe_3O_4 @carbon nanorods for application in lithium ion batteries. *J Phys Chem C* 2011;115:9814–20.
 - [14] Wu P, Du N, Zhang H, Yu JX, Yang DR. Carbon nanocapsules as nanoreactors for controllable synthesis of encapsulated iron and iron oxides: magnetic properties and reversible lithium storage. *J Phys Chem C* 2011;115:3612–20.
 - [15] Yang ZC, Shen JG, Archer LA. An in situ method of creating metal oxide-carbon composites and their application as anode materials for lithium-ion batteries. *J Mater Chem* 2011;21:11092–7.
 - [16] Piao YZ, Kim HS, Sung YE, Hyeon T. Facile scalable synthesis of magnetite nanocrystals embedded in carbon matrix as superior anode materials for lithium-ion batteries. *Chem Commun* 2010;46:118–20.
 - [17] Yoon T, Chae C, Sun YK, Zhao X, Kung HH, Lee JK. Bottom-up in situ formation of Fe_3O_4 nanocrystals in a porous carbon foam for lithium-ion battery anodes. *J Mater Chem* 2011;21:17325–30.
 - [18] Kang E, Jung YS, Cavanagh AS, Kim GH, George SM, Dillon AC, et al. Fe_3O_4 nanoparticles confined in mesocellular carbon foam for high performance anode materials for lithium-ion batteries. *Adv Funct Mater* 2011;21:2430–8.
 - [19] Wang JZ, Zhong C, Wexler D, Idris NH, Wang ZX, Chen LQ, et al. Graphene-encapsulated Fe_3O_4 nanoparticles with 3D laminated structure as superior anode in lithium ion batteries. *Chem Eur J* 2011;17:661–7.
 - [20] Zhou GM, Wang DW, Li F, Zhang LL, Li N, Wu ZS, et al. Graphene-wrapped Fe_3O_4 anode material with improved reversible capacity and cyclic stability for lithium ion batteries. *Chem Mater* 2010;22:5306–13.
 - [21] Zhang M, Lei DN, Yin XM, Chen LB, Li QH, Wang YG, et al. Magnetite/graphene composites: microwave irradiation synthesis and enhanced cycling and rate performances for lithium ion batteries. *J Mater Chem* 2010;20:5538–43.
 - [22] Baek S, Yu SH, Park SK, Pucci A, Marichy C, Lee DC, et al. A one-pot microwave-assisted non-aqueous sol-gel approach to metal oxide/graphene nanocomposites for Li-ion batteries. *RSC Adv* 2011;1:1687–90.
 - [23] Li BJ, Cao HQ, Shao J, Qu MZ. Enhanced anode performances of the Fe_3O_4 -Carbon-rGO three dimensional composite in lithium ion batteries. *Chem Commun* 2011;47:10374–6.
 - [24] Li BJ, Cao HQ, Shao J, Qu MZ, Warner JH. Superparamagnetic Fe_3O_4 nanocrystals@graphene composites for energy storage devices. *J Mater Chem* 2011;21:5069–75.
 - [25] Ban CM, Wu ZC, Gillaspie DT, Chen L, Yan YF, Blackburn JL, et al. Nanostructured Fe_3O_4 /SWNT electrode: binder-free and high-rate Li-ion anode. *Adv Mater* 2010;22:E145–9.
 - [26] Sun XM, Li YD. Colloidal carbon spheres and their core/shell structures with noble-metal nanoparticles. *Angew Chem Int Ed* 2004;43:597–601.
 - [27] Sevilla M, Fuertes AB. Chemical and structural properties of carbonaceous products obtained by hydrothermal carbonization of saccharides. *Chem Eur J* 2009;15:4195–203.
 - [28] Ryu J, Suh YW, Suh DJ, Ahn DJ. Hydrothermal preparation of carbon microspheres from mono-saccharides and phenolic compounds. *Carbon* 2010;48:1990–8.
 - [29] Sun XM, Li YD. Ag@C core/shell structured nanoparticles: controlled synthesis, characterization, and assembly. *Langmuir* 2005;21:6019–24.
 - [30] Yu SH, Cui X, Li L, Li K, Yu B, Antonietti M. From starch to metal/carbon hybrid nanostructures: hydrothermal metal-catalyzed carbonization. *Adv Mater* 2004;16:1636–40.
 - [31] Zhong ZY, Ho J, Teo J, Shen SC, Gedanken A. Synthesis of porous $\alpha\text{-Fe}_2\text{O}_3$ nanorods and deposition of very small gold particles in the pores for catalytic oxidation of CO. *Chem Mater* 2007;19:4776–82.
 - [32] Parks GA. The isoelectric points of solid oxides, solid hydroxides, and aqueous hydroxo complex systems. *Chem Rev* 1965;65:177–98.
 - [33] Yu DH, Aihara M, Antal Jr MJ. Hydrogen production by steam reforming glucose in supercritical water. *Energy Fuels* 1993;7:574–7.
 - [34] Wang DW, Li F, Liu M, Lu GQ, Cheng HM. 3D aperiodic hierarchical porous graphitic carbon material for high-rate electrochemical capacitive energy storage. *Angew Chem Int Ed* 2008;47:373–6.
 - [35] Wu ZS, Ren WC, Wen L, Gao LB, Zhao JP, Chen ZP, et al. Graphene anchored with Co_3O_4 nanoparticles as anode of lithium ion batteries with enhanced reversible capacity and cyclic performance. *ACS Nano* 2010;4:3187–94.
 - [36] Zhou GM, Wang DW, Yin LC, Li N, Li F, Cheng HM. Oxygen bridges between NiO nanosheets and graphene for improvement of lithium storage. *ACS Nano* 2012;6:3214–23.
 - [37] Obrovac MN, Dahn JR. Implications of finite-size and surface effects on nanosize intercalation materials. *Phys Rev B* 2000;61:6713–9.
 - [38] Van der Ven A, Wagemaker M. Effect of surface energies and nano-particle size distribution on open circuit voltage of Li-electrodes. *Electrochem Commun* 2009;11:881–4.
 - [39] Delmer O, Balaya P, Kienle L, Maier J. Enhanced potential of amorphous electrode materials: case study of RuO_2 . *Adv Mater* 2008;20:501–5.
 - [40] Prosini PP, Lisi M, Zane D, Pasquali M. Determination of the chemical diffusion coefficient of lithium in LiFePO_4 . *Solid State Ionics* 2002;148:45–51.